J Solid State Electrochem (2012) 16:2095–2102
DOI 10.1007/s10008-011-1620-4

ORIGINAL PAPER

Nanostructured Fe_2O_3–graphene composite as a novel electrode material for supercapacitors

Dewei Wang · Yuqi Li · Qihua Wang · Tingmei Wang

Received: 23 September 2011 / Revised: 4 December 2011 / Accepted: 9 December 2011 / Published online: 28 December 2011

Abstract Nanostructured Fe_2O_3–graphene composite was successfully fabricated through a facile solution-based route under mild hydrothermal conditions. Well-crystalline Fe_2O_3 nanoparticles with 30–60 nm in size are highly encapsulated in graphene nanosheet matrix, as demonstrated by various characterization techniques. As electrode materials for supercapacitors, the as-obtained Fe_2O_3–graphene nanocomposite exhibits large specific capacitance (151.8 F g^{-1} at 1 A g^{-1}), good rate capability (120 F g^{-1} at 6 A g^{-1}), and excellent cyclability. The significantly enhanced electrochemical performance compared with pure graphene and Fe_2O_3 nanoparticles may be attributed to the positive synergetic effect between Fe_2O_3 and graphene. In virtue of their superior electrochemical performance, they will be promising electrode materials for high-performance supercapacitors applications.

Keywords Fe_2O_3 · Graphene · Nanoparticles · Electrochemical performance

Electronic supplementary material The online version of this article (doi:10.1007/s10008-011-1620-4) contains supplementary material, which is available to authorized users.

D. Wang · Y. Li · Q. Wang (✉) · T. Wang
State Key Laboratory of Solid Lubrication, Lanzhou Institute of Chemical Physics, Chinese Academy of Sciences, Lanzhou 730000, People's Republic of China
e-mail: Wangqh@lzb.ac.cn

D. Wang · Y. Li
Graduate School of Chinese Academy of Sciences, Beijing 10039, People's Republic of China

Introduction

Energy storage and conversion is one of the most important issues in the twenty-first century [1, 2]. In this context, the research and development of new, low-cost, and environmental friendly energy storage system have received paramount currently attention. Supercapacitors (also called electrochemical capacitors or ultracapacitors), as one of the most promising electrochemical energy storage systems, are rapidly gaining momentum, particularly in the field of portable electronic devices, electric vehicles, and hybrid electric vehicles due to their high power density and long cycle life compared with secondary batteries and their higher energy density compared with electrostatic and electrolytic capacitors [3–7]. Generally, supercapacitors can be simply classified as electric double-layer capacitors (EDLCs) and pseudocapacitors depending on the nature of charge storage mechanism [3]. The charge storage mechanism in EDLCs is through electrostatic forces based on electrical double layers formed at the interface between an electrode and electrolyte [8]. EDLCs using carbon-based materials usually have high power density but suffer from low energy density [3, 9]. In contrast, charge storage mechanism in pseudocapacitors is raising from fast Faradaic redox reactions between the electrolyte and the electrode [3, 10]. The specific capacitance values based on fast Faradaic redox reactions are usually many times greater than that of the EDLCs therefore the key point for the development of high-performance supercapacitors [3, 11].

Electrode materials for redox pseudocapacitors are typically conductive polymers or transition metal oxides. Although conductive polymers have large specific values, the degradation of the conducting polymer material as a result of swelling and shrinkage of electroactive polymers during

cycling limited their applications significantly [12]. Ruthenium oxide (RuO_2) has a good pseudocapacitance (as high as 720 F g^{-1}) and high electronic conductivity but its toxic nature and high cost limit its commercial applications greatly [13]. Therefore, numerous studies have been carried out to find new materials with superior capacitive behavior but much cheaper. In this regard, transition metal oxides such as, manganese oxides, nickel oxides, and cobalt oxides are intensively investigated as potential materials for electrochemical capacitors [14–20]. Although these classes of metal oxides are well-established for electrochemical energy-storage applications, exploration of alternative electrode material with a combination of low cost and improved performances is particularly interesting. Iron oxides have been considered as one of the most promising pseudocapacitor electrode materials with respect to both its specific capacitance and cost effectiveness [21]. For example, Fe_3O_4 and γ-Fe_2O_3 exhibit good pseudocapacitor behavior in alkaline electrolyte with the capacitances of 5–500 F g^{-1} depending on the electrolyte, cell–design, structure, and morphology. However, the high-rate charge–discharge performance and cycle stability are not satisfied because of their poor electrical conductivity and metastability [22, 23]. Recent studies show that hematite (α-Fe_2O_3) nanostructures can be used as electrode materials for supercapacitors. For instance, nanostructured iron oxides (α-Fe_2O_3) film was electrodeposited anodically onto nickel substrate for ECs has been developed by Wu and co-workers [24]. They found that the electrochemical capacitive performance of the film depends on morphologies. Recently, we developed a morphological–conserved route for the synthesis of mesoporous α-Fe_2O_3 nanostructures with controllable shapes for supercapacitors applications [25]. The mesoporous multi-layered nanosheets have the maximum specific capacitance value of 116.25 F g^{-1} at 0.75 A g^{-1} and the specific capacitance drops to 86.25 F g^{-1} after 1,000 continuous charge–discharge cycles. Very recently, Huang and co-worker successfully fabricated highly ordered α-Fe_2O_3 nanotube arrays through anodization method on iron foils for supercapacitors [26]. The as-prepared α-Fe_2O_3 nanotube arrays exhibit high specific capacitance value of 138 F g^{-1} at 1.3 A g^{-1}. Strikingly, the unique nanostructures of the α-Fe_2O_3 nanotube arrays also present remarkable rate capability (91 F g^{-1} at 12.8 A g^{-1}) and good cycling stability (the capacitance retention close to 89% after 500 cycles). The superior electrochemical performance of mesoporous nanostructures and nanotube arrays can be attributed to its large specific surface areas for electrolyte accessibility, shorter pathway for rapid ion diffusion, and more active sites for fast Faradaic redox reactions. Nevertheless, the synthesis of these novel structures is rather complex and difficult to control. Another option that can improve the electrochemical performance is to combine α-Fe_2O_3 with other components with good conductivity to facilitate the electron transfer between the active materials and the current collector. For example, Long and co-workers described a simple electroless deposition of conformal nanoscale iron oxide on carbon nanofoams for ECs [27]. The resulting FeO_x–carbon nanofoams can deliver specific capacitance value of 84 and 300 F g^{-1} when normalized to the content of FeO_x. In addition, the as-obtained FeO_x–carbon nanofoams have good capacity retention (capacitance fading <20% over 1,000 consecutive cycles) by the addition of borate to buffer the Li_2SO_4 electrolyte to suppress the electrochemical dissolution of the FeO_x. Despite this success, there still remains much interest in exploring simpler and versatile synthetic route for the synthesis of α-Fe_2O_3-based composites with enhanced electrochemical performance.

Graphene, a unique single-layer of carbon atoms tightly packed into a two–dimensional honeycomb sp^2 carbon lattice, has attracted tremendous attention in energy storage devices as a result of its huge specific surface area, good chemical stability, and remarkable electrical conductivity [28–31]. Such merits suggest that graphene sheets can be used as matrices for hosting active nanomaterials to improve their electrochemical performance results from the synergistic effects of their components [31–35]. For example, Ruoff and co-workers demonstrated, for the first time, that reduced graphene oxide–Fe_2O_3 composites can be used as the excellent anode material for Li-ion batteries [32]. The reduced graphene oxide–Fe_2O_3 composites exhibit large specific capacity, good cycling performance and rate capability because of the positive synergistic effect of reduced graphene oxide and Fe_2O_3. Dai and co-workers reported a novel solution-based route for the synthesis of $Ni(OH)_2$–graphene composites for electrochemical pseudocapacitors with potentially high energy densities, extraordinary power densities, and long cycle life[33]. Enlightened by these pioneer works, it is believed that the nanostructured Fe_2O_3–graphene composite will be a promising candidate for high-performance supercapacitors. However, to our best knowledge, employing Fe_2O_3–graphene composites as electrode materials for supercapacitors have not been reported. Herein, we demonstrate the successful preparation of Fe_2O_3–graphene composites via a facile one-step solution-based route under mild conditions. Significantly, the resulting Fe_2O_3–graphene composites exhibit good pseudocapacitive behavior in terms of highly specific capacitance, good rate capability, and excellent cyclability.

Experimental section

All chemical reagents (analytical grade) were used as received without further purification. Deionized water was used throughout.

Preparation of GO Graphite oxide (GO) was synthesized from pristine graphite powder based on a modified Hummers method [34] (Fig. S1 in the Electronic Supplementary Material (ESM)). Then, 20 mg of GO and 40 mL of water were ultrasonicated in a beaker for 90 min in order to fully exfoliate the graphite oxide to GO sheets. Finally, a homogeneous GO aqueous dispersion (0.5 mg mL^{-1}) was obtained.

Preparation of Fe_2O_3–graphene nanocomposites In a typical procedure, an aqueous solution (10 mL) of $FeCl_3{\cdot}6H_2O$ (0.6 mmol) was added into an aqueous suspension of GO (40 mL). After continuous stirring for 2 h, 10 mL of NaOH (1.2 mmol) aqueous solution was added dropwise into the above mixture. Finally, the mixture was sealed in a Teflon-lined stainless steel autoclave for hydrothermal reaction at 180 °C for 12 h. The final product was washed several time with water and ethanol, and then dried at 80 °C for 12 h. For comparison, Fe_2O_3 particles and graphene were also prepared in the same conditions but without the presence of GO or $FeCl_3$.

Characterizations and electrochemical tests. The phase structure of the products was measured by powder X-ray diffraction (XRD) experiments on a RigaKu D/max–RB diffractometer with Ni-filtered graphite–monochromatized CuKα radiation (λ=1.54056 Å). The morphology and microstructure of the products were characterized using a transmission electron microscope (TEM; FEI, Tecnai 30) with an accelerating voltage of 300 kV and a field-emission scanning electron microscope (FESEM; JEOL JSM-6701F). Fourier transform infrared (FTIR) spectra are recorded on IFS 66v/s FTIR spectrophotometer from 4,000 to 400 cm^{-1} at room temperature using KBr pellet technique. X-ray photoelectron spectrometer (XPS; X-ray monochromatisation, Thermon Scientific) was carried out with Al Kα as the excitation source; the binding energies obtained in the XPS analysis were calibrated against the C 1 s peak at 285.0 eV. The specific surface area was estimated by the Brunauer–Emmet–Teller method based on nitrogen absorption–desorption (Micromeritics ASAP 2020). Thermogravimetric (TG)–differential scanning calorimetric (DSC) analysis of the cobalt oxalate precursor was performed on a Netzsch STA 449 F3 thermogravimetric analyzer (Germany). The TG and DSC curves were recorded in a dynamic atmosphere at a heating rate of 10 °C min^{-1} in the temperature range of 30–800 °C.

The working electrodes were prepared by mixing the electroactive material (80 wt.%), acetylene black (15 wt. %), and poly(tetrafluoroethylene) (5 wt.%) binders in ethanol to form a homogeneous slurry, which was then pressed onto a nickel grid (about 1×1 cm^2) and dried at 60 °C overnight. The electrochemical measurements were done in a three-electrode cell with Pt foil (1×1 cm^2) as the counter electrode and a saturated calomel electrode (SCE) as the reference electrode. The mass of active materials in working electrode was 6 mg. The used electrolyte was 2 M aqueous KOH solution. Cyclic voltammetry (CV) tests were done between −0.85 and 0 V (vs. SCE) at different scan rates. The long-term galvanostatic charge–discharge was evaluated with a LAND CT2001A multichannel galvanostat in the potential range of −0.85–0 V (vs. SCE) at a current density of 2 A g^{-1}. CV and chronopotentiometry tests were employed on an electrochemical workstation (CHI 660B, Chenhua, Shanghai). Before electrochemical tests, the working electrodes were aged for 12 h to ensure good soakage of the electroactive material in the electrolyte [35].

Results and discussion

GO are highly negatively charged result from numerous oxygen-containing functional groups attached to the surface and edge of carbon sheets [28]. They readily exfoliated in water to yield a stable dispersions consisting mostly of single-layer sheets, which are referred to as graphene oxide sheets [36] (Fig. S2 in the ESM). The positive charged Fe ions will adsorb onto the surface of graphene oxide nanosheets by strong electrostatic interactions [28, 31, 37–39]. After continuous stirring, almost all of the Fe ions will adsorb onto GO surface to form Fe ions–GO mixtures. NaOH was used as the precipitant to conversion of Fe ions–GO into $Fe(OH)_3$–GO. The $Fe(OH)_3$ particles produced anchor onto the surfaces of the GO sheets through oxygen-containing functional groups, such as carboxyl, hydroxyl, and epoxy [28, 32, 38]. Under hydrothermal conditions, $Fe(OH)_3$ decomposes to Fe_2O_3 while GO is converted into graphene via dehydration and dehydroxylation [28, 32]. Finally, Fe_2O_3–graphene composites formed after hydrothermal treatment.

The as-prepared Fe_2O_3–graphene composites were first characterized by X-ray diffraction to identify its structure and the diffraction pattern is presented in Fig. 1. All peaks could be readily indexed as a pure rhombohedral phase of α-Fe_2O_3 (hematite, space group: *R3c*) with lattice constants a=5.03 Å and c=13.67 Å, which are consistent with the values given in the standard card (JCPDS no. 33-0664). No other crystalline phases were observed, which suggests the high purity of the as-prepared product. Moreover, the XRD diffraction peaks are relatively broad, indicating that the crystals constituting the products are of small sizes. Moreover, no stacking peak of graphene sheets is detected, suggesting that the graphene sheets are highly disordered stacking with a low degree of graphitization [32, 37]. These results indicate that the as-obtained composite consists of disorderedly stacked graphene and well-crystallized Fe_2O_3 nanoparticles. Comparing with bare Fe_2O_3, the weakening

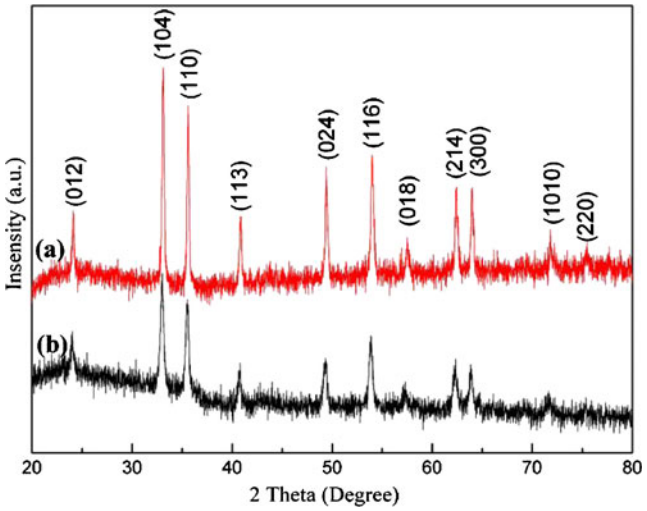

Fig. 1 XRD patterns of the Fe_2O_3 nanoparticles (**a**) and Fe_2O_3–graphene nanocomposites (**b**)

of the diffraction intensity for Fe_2O_3–graphene composites probably result from the GO surface interacts strongly with the coated species, providing pinning forces to the small particles to hinder diffusion and recrystallization [40]. For quantifying the amount of graphene in the Fe_2O_3–graphene composites, thermogravimetric analysis was carried out in air. As can be seen from Fig. S3, the Fe_2O_3–graphene composites show a rapid mass loss between 350 and 450 °C with an exothermal peak in the DSC curve. The weight loss of this step is about 17.45%, indicating that the amount of graphene in the Fe_2O_3–graphene composite is about 17.45%. The presence of graphene and Fe_2O_3 nanoparticles in the composites was also confirmed by FTIR spectroscopy analysis. For GO, the bands at 1,071, 1,230, 1,380, and 1,734 cm^{-1} (Fig. 2a), which correspond to C–O stretching vibrations, C–OH

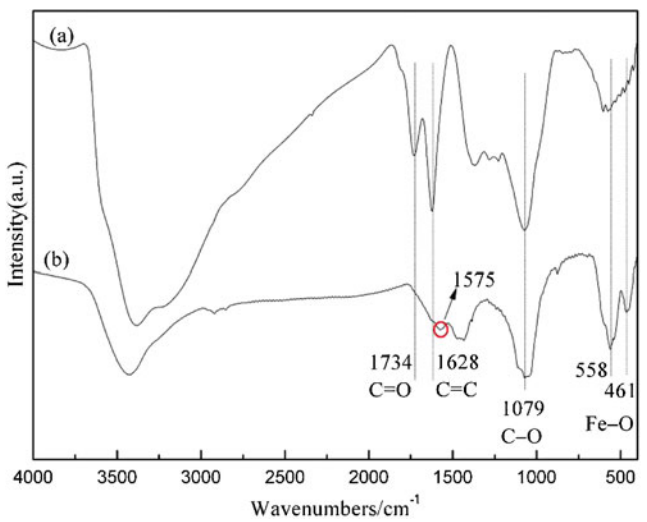

Fig. 2 FTIR spectrum of the GO (**a**) and Fe_2O_3–graphene nanocomposites (**b**)

stretching peak, C–O–H deformation peak, and C–O stretching of COOH groups, respectively [28]. Compared with GO, two new peaks located at 558 and 461 cm^{-1} should be the stretching vibration of Fe–O [41]. This values shift to higher wavenumbers compared with that of 540 and 455 cm^{-1} reported for the stretching mode of Fe–O in bulk [42]. Moreover, all of these absorption peaks related to oxidized groups decreased significantly in the FTIR spectrum of Fe_2O_3–graphene composites, indicating the reduction of GO and restoration of the conjugated aromatic system [28, 38]. In addition, a new absorption band that appears at 1,575 cm^{-1} corresponds to the aromatic skeletal of C=C stretching vibration of the graphene sheets further confirm the reduction of GO. The chemical bonding states in the product were further provided by XPS measurements, as shown in Fig. 3. The Fe 2p XPS spectra of the sample exhibit two peaks at 724.6 and 711.2 eV, corresponding to the Fe $2p_{1/2}$ and Fe $2p_{3/2}$ spin–orbit peaks of Fe_2O_3 (Fig. 3b). Moreover, a satellite peak at 718.9 eV (indicated by a circle), which is the characteristic of Fe_2O_3 [32]. The peak at 530.3 eV in the O 1 s spectra corresponds to the oxygen species in the metal oxide (Fig. 3c). Another peak at 532.1 eV indicates the presence of residual oxygen–containing groups (such as C–O–C and –COOH) bonded with C atoms in graphene [37]. Compared with C 1 s of GO (Fig. S4 in the ESM), the intensities of all of the C1s peaks of the carbons binding to oxygen and the peak of sp^3 carbon, especially the peak of C–O (epoxy and alkoxy), decreased dramatically revealing that most of the oxygen containing functional groups are successfully removed and the conjugated graphene networks are partially restored.

In order to investigate the surface area of the as-prepared Fe_2O_3–graphene composites, N_2 adsorption/desorption isotherms were carried out, as shown in Fig. 4a. According to the IUPAC classification, the isotherm can be classified as type IV with H3 type hysteresis behavior with an evident hysteresis loop. In particular, when the relative pressure (P/P_0) is higher than 0.9, a steep increase appears, indicating the presence of macropores. For pure Fe_2O_3 nanoparticles, a small step of N_2 adsorption and desorption branches occurs at the relative high pressure (P/P_0), indicating the pores mainly comes from the voids among the nanoparticles (Fig. 4b). The specific surface area of Fe_2O_3–graphene is 121.35 $m^2\ g^{-1}$, which is larger than pure Fe_2O_3 NPs (24.55 $m^2\ g^{-1}$). The large specific surface areas will undoubtedly shorten the ion diffusion paths and enhance the utilization of active materials, which can contribute to an improved pseudocapacitive performance.

Figure 5a and b are the low and high magnification TEM images of the as-obtained Fe_2O_3–graphene nanocomposites (also see Fig. S5 in the ESM). As can be seen in Fig. 5a, a sheet-like shape of graphene with a size larger than 2 μm is uniformly deposited with numerous nanoparticles. From the

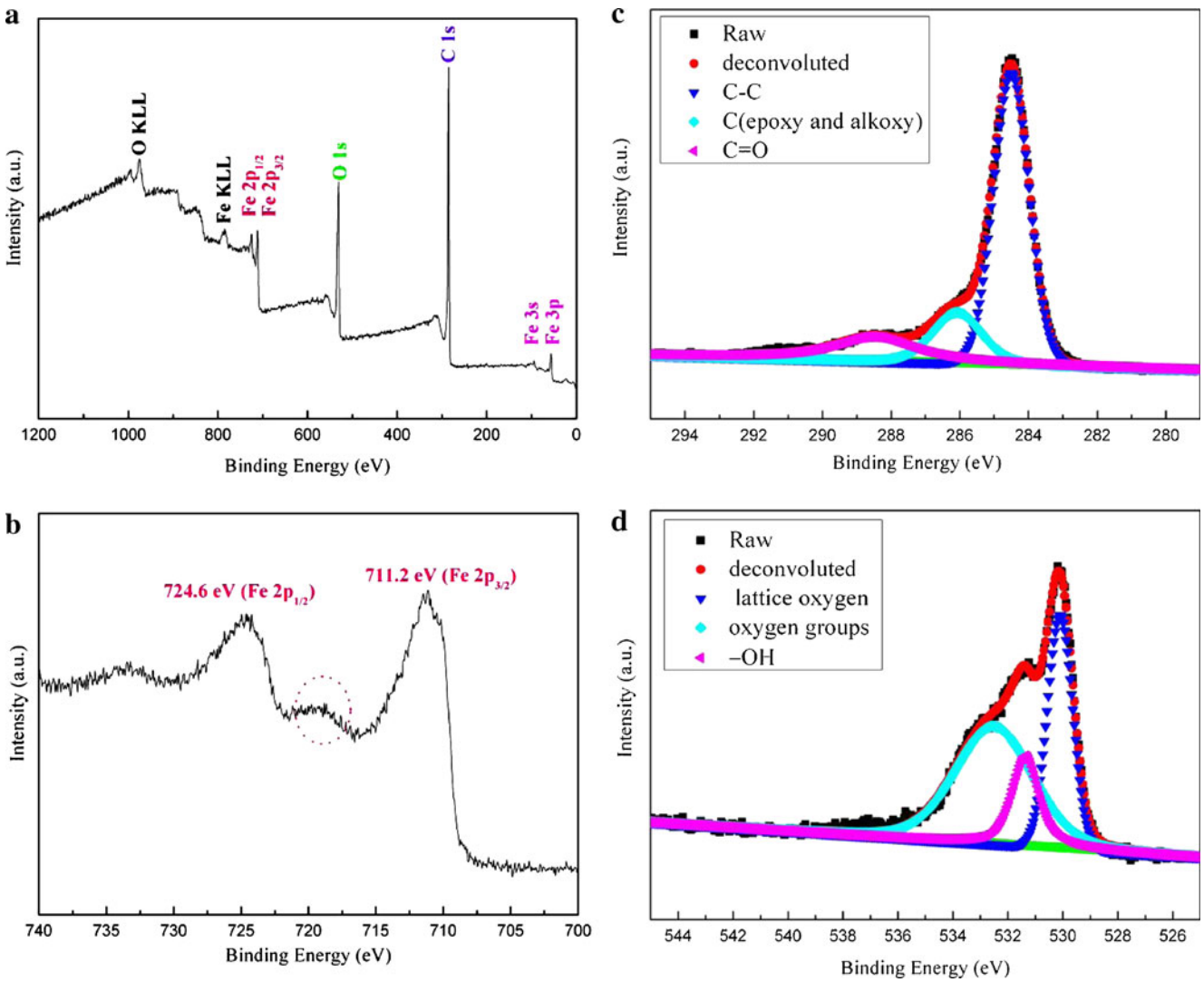

Fig. 3 XPS spectra of Fe_2O_3–graphene nanocomposites **a** wide scan, **b** Fe 2p, **c** C 1 s, and **d** O 1 s spectra of the Fe_2O_3–graphene nanocomposites

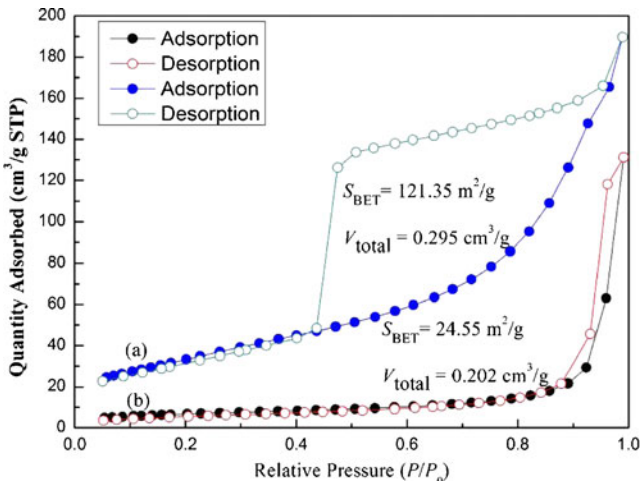

Fig. 4 N_2 adsorption–desorption isotherms of Fe_2O_3–graphene nanocomposites (**a**) and Fe_2O_3 nanoparticles (**b**)

high magnification TEM image (Fig. 5b), it can be seen clearly that the Fe_2O_3 with a size of 30–60 nm are homogeneously deposited on the thin graphene layers. Graphene sheets show wrinkled or crumpled thin paper-like structure with a lot of folds at the edge. High-resolution TEM (HRTEM) image (Fig. 5c) clearly demonstrates that the well-crystallized and single-crystalline nature of Fe_2O_3 nanoparticles in the Fe_2O_3–graphene composite. The lattice fringes with a distance of 0.252 nm were clearly observed in the Fig. 5c, which can be indexed as the (1 1 0) plane of α-Fe_2O_3. The chemical composition of the obtained Fe_2O_3–graphene nanocomposites was also determined by energy-dispersive X-ray spectroscopy (EDX) analysis attached to the TEM (Fig. 5d). The result shows the presence of Fe, O, C, and Cu peaks, the signals of Cu element originated from the supporting TEM grid during the measurement. Based on the above analysis, it is unambiguously demonstrated that Fe_2O_3 nanoparticles have been successfully attached onto

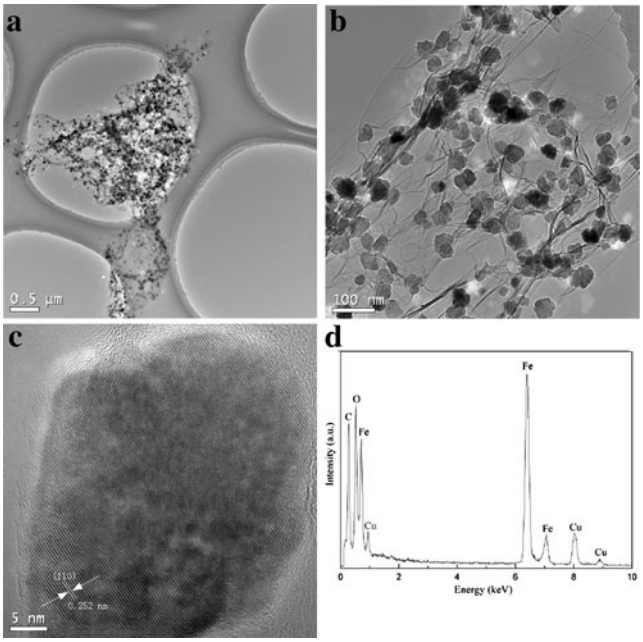

Fig. 5 Typical TEM images of the as-obtained Fe_2O_3–graphene nanocomposites **a** lower magnification and **b** higher magnification, **c** HRTEM image, and **d** EDX spectrum

the surfaces of graphene sheets. It is worthwhile to note that the interaction between nanoparticles and graphene sheets is quite strong, which cannot be destroyed even after a long time of ultrasound irradiation. The intimate contact between the Fe_2O_3 nanoparticles and graphene sheets enables fast electronic and ionic transport through the active materials to charge collector and thus improve the electrochemical performance [32, 37]. Moreover, Fe_2O_3 nanoparticles on the surface of graphene sheets can act as spacers to efficiently prevent the aggregation of the nanoparticles as well as the restacking of graphene sheets, avoiding/weakening the loss of their high active surface area [37]. FESEM images of the pure Fe_2O_3 obtained at the same reaction conditions are shown in Fig. S6. The as-prepared Fe_2O_3 nanoparticles are 20–100 nm in size agglomerated severely into several micrometers. Figure S7 shows the FESEM image of the as-synthesized graphene. It is evident that pure graphene has some wrinkles and folds but not transparent suggesting graphene nanosheets restack each other greatly during the hydrothermal reduction process, which is consistent with the XRD result (Fig. S7 in the ESM).

CV and galvanostatic charge–discharge measurements were examined in a half-cell configuration with three-electrode mode to evaluate the electrochemical properties of the Fe_2O_3–graphene composites. Figure 6a shows the representative CV curves of the Fe_2O_3–graphene composites at different scan rates in 2 M KOH electrolyte with a potential window between –0.85 and 0 V (vs. SCE). The rectangular and symmetric with two couple well-defined redox reaction peaks in CV curves indicated the combination of both double-

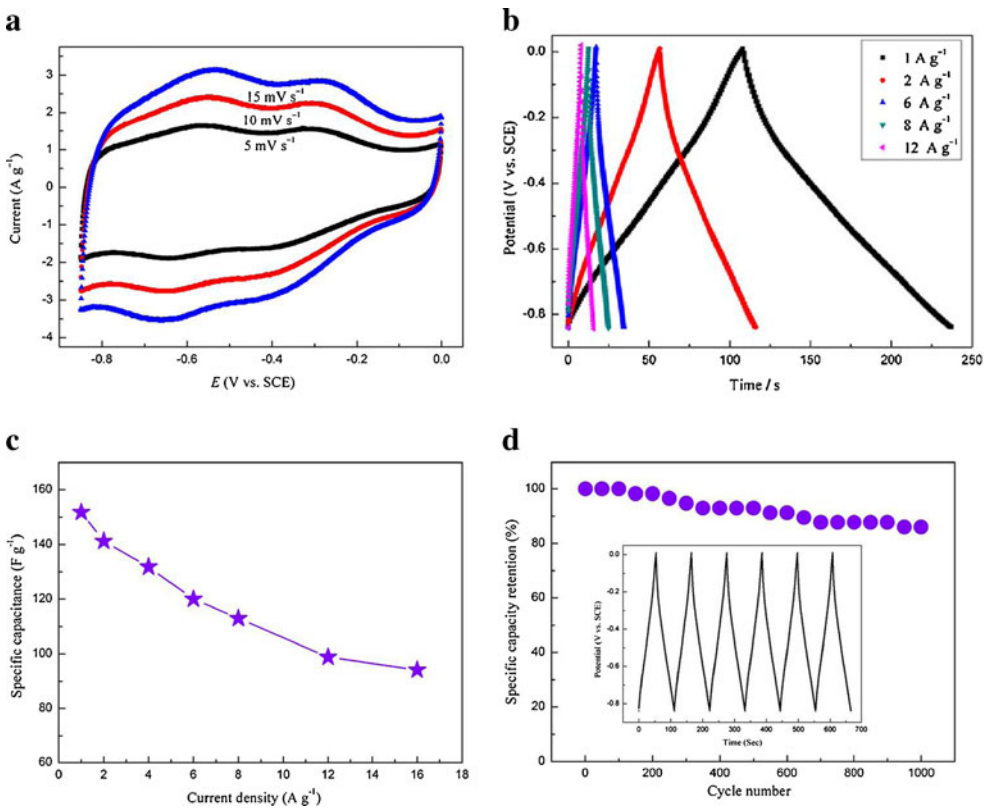

Fig. 6 Cyclic voltammograms of the Fe_2O_3–graphene electrode at the scan rate from 5 to 15 mV s^{-1} (**a**) and **b** charge–discharge curves of the Fe_2O_3–graphene electrode at different current densities at the potential range of −0 85 to 0 V in 2 M KOH aqueous electrolyte, **c** plot of specific capacitance as a function of current density, and **d** capacitance retention of the Fe_2O_3–graphene electrode as a function of cycle number The inserts show the charge–discharge profiles of the first six charge–discharge cycles at the current density of 2 A g^{-1} with the voltage window from −0 85 to 0 V

layer capacitive from graphene and pseudocapacitive behavior from Fe_2O_3. The pseudocapacitance is rising from the reaction between Fe^{3+} and electrolyte, which are mainly governed by the intercalation and deintercalation of K^+ species within can intercalate into the interlayer, the tunnels, and the holes in the crystal structure [25, 43]. The peak current increases with increasing scan rate from 5 to 15 mV s^{-1} but the shape of the CV changed slightly indicating a small equivalent series resistance and weak polarization of the electrodes [44]. Furthermore, the almost linear (quasi-linear) relationship of the plot of peak current versus the square root of scan rate (Fig. S8 in the ESM), indicating a fast electron transfer rate during the electrochemical reaction, and thus the electrode process is rather a diffusion controlled than a kinetic one.

The charge–discharge behavior of the as-prepared Fe_2O_3–graphene electrode was evaluated by galvanostatic charge–discharge cycling at different current densities in KOH solution (2 M) with the potential ranges between −0.85 and 0 V (vs. SCE). Pure graphene and Fe_2O_3 nanoparticles prepared by the same procedure under the same electrochemical conditions were also studied for comparison (Fig. S9 in the ESM). Obviously, Fe_2O_3–graphene electrode shows a longer charge–discharge time under the same galvanostatic charge–discharge process, implying a larger capacitance than pure graphene and Fe_2O_3 nanoparticles. Moreover, the charging curves are somewhat mirror-symmetrical to their discharging counterparts indicating the Fe_2O_3–graphene electrode has high electrochemical reversibility and excellent capacitive characteristics [35]. The specific capacitances were calculated from the galvanostatic discharge curves using the equation: $C = It/(\Delta Vm)$, where I is the current applied, t is the total discharge time, ΔV is the potential drop during discharging, and m is the mass of the sample on one electrode. On the basis of this equation, the specific capacitance values of Fe_2O_3–graphene composite, pure graphene and Fe_2O_3 nanoparticles can thus be calculated from the discharge curves to be 141.2, 54.1, and 18.2 F g^{-1}, respectively. It is worth to note that the background capacitance of nickel foam (including acetylene black) was negligible (Fig. S9 in the ESM), suggesting that the capacitance mainly from Fe_2O_3–graphene composite. Importantly, the Fe_2O_3–graphene composite exhibits excellent rate capability. Figure 6b shows representative charge–discharge profiles of the Fe_2O_3–graphene electrode at various current densities. A specific capacitance of 151.8 F g^{-1} can be achieved at 1 A g^{-1} and 120 F g^{-1} at 6 A g^{-1}. When the current density further increased to 16 A g^{-1}, the specific capacitance can still remain at a high level of 94 F g^{-1} with a good retention above 62% (Fig. 6c). The super high-rate charge–discharge capability implying that the unique structure can sustain the rapid transport of electrolyte ions and electron throughout the electrode and ensure the highly efficient of utilization of pseudo and double-layer capacitance [32, 37, 45].

The electrochemical stability of the Fe_2O_3–graphene electrode is investigated by chronopotentiometry measurement in the range of −0.85–0 V at 2 A g^{-1} in 2 M KOH aqueous solution. As shown in Fig. 6d, the specific capacitance only decreases by 14% of the initial capacitance after 1,000 cycles, revealing the excellent electrochemical stability of the Fe_2O_3–graphene electrode. To the best of our knowledge, this is the best report for the cycle stability of Fe_2O_3-based electrode. Previous studies employing Li_2SO_4 as electrolyte but the acidity of the lithium sulfate electrolyte is expected to promote reductive dissolution of the Fe_2O_3 when cycled to progressively negative potentials, with the formation of soluble Fe^{2+} species inevitably lead to capacitance loss [27]. In this work, KOH used as electrolyte instead of Li_2SO_4 because of the K^+ has a similar hydration ions radius with Li^+ and Fe_2O_3 also has a good stability in alkaline electrolyte than in acidic environments. More importantly, the residual functional groups attached to graphene nanosheets are more chemically active in alkali electrolytes where redox reactions occurred, which will contribute to the total pseudocapacitance [46]. The excellent pseudocapacitive performance of the Fe_2O_3–graphene composite electrode is probably attributed to the positive synergistic effects between the Fe_2O_3 and graphene. First, the incorporation of Fe_2O_3 nanoparticles into graphene cannot only inhibit the stacking/agglomerating of graphene nanosheets but also reduce the aggregation of the nanoparticles made the nearly every Fe_2O_3 nanoparticle accessible to the electronic and ionic transport pathways resulting in high double–layer capacitance, and importantly, enhancing the utilization of active materials [28]. Second, the large distance between neighboring graphene nanosheets provide enough void spaces to buffer volume change during the redox reaction, and endow good electrical contact with the nanoparticles upon cycling [32, 37]. Third, the unique structure can facilitate the diffusion and migration of the electrolyte ions that can increase the specific capacitance value and improve the high-rate charge–discharge performance [38, 39]. Finally, graphene also provides a highly conductive network for electron transport during the charge and discharge processes, thus reducing the polarization of the electrodes [44–46].

Conclusions

In summary, we have developed an efficient solution-based route for the synthesis of nanostructured Fe_2O_3–graphene composite under hydrothermal conditions. Various measurements confirm that well-crystalline Fe_2O_3 nanoparticles with 30–60 nm in size are highly encapsulated in a graphene nanosheet matrix. The electrochemical properties of the Fe_2O_3–graphene composites were measured by cyclic voltammogram and galvanostatic charge–discharge studies. Results show that the Fe_2O_3–graphene nanocomposite

exhibits excellent electrochemical performance as an electrode for supercapacitors in terms of specific capacitance, rate capability, and cyclability. The superior electrochemical performance of the Fe_2O_3–graphene is probably attributed to its unique nanostructure, which intimately combines the conductive graphene network with uniformly dispersed Fe_2O_3 nanoparticles.

Acknowledgments The authors would like to acknowledge the financial support of the National Science Foundation for Distinguished Young Scholars of China (grant no. 51025517), and National Defense Basic Scientific Research Project (A1320110011).

References

1. Arico AS, Bruce P, Scrosati B, Tarascon JM, Schalkwijk WV (2005) Nat Mater 4:366–377
2. Simon P, Gogotsi Y (2008) Nat Mater 7:845–854
3. Conway BE (1999) Electrochemical supercapacitors. Kluwer Academic, New York
4. Miller JR, Simon P (2008) Science 321:651–652
5. Malachi N, Soffer A, Aurbach D (2011) J Solid State Electrochem 15:1563–1578
6. Brezesinski T, Wang J, Tolbert SH, Dunn B (2010) Nat Mater 9:146–151
7. Wang HB, Liu ZH, Chen X, Han PX, Dong SM, Cui GL (2011) J Solid State Electrochem 15:1179–1184
8. Baughman RH, Zakhidov AA, de Heer WA (2002) Science 297:787–792
9. Liu R, Lee SB (2008) J Am Chem Soc 130:2942–2943
10. Stoller MD, Park SJ, Zhu YW, An JH, Ruoff RS (2008) Nano Lett 8:3498–3502
11. Zhao X, Sanchez BM, Dobson P, Grant P (2011) Nanoscale 3:839–855
12. Winter M, Brodd RJ (2004) Chem Rev 104:4245–4269
13. Zheng JP, Jow TR (1995) J Electrochem Soc 142:L6–L8
14. Toon YS, Cho WI, Lim JH, Choi DJ (2001) J Power Sources 101:126–129
15. Liu KC, Anderson MA (1996) J Electrochem Soc 143:124–130
16. Toupin M, Brousse T, Belanger D (2002) Chem Mater 14:3946–3950
17. Wei WF, Cui XW, Chen WX, Ivey DG (2011) Chem Soc Rev 40:1697–1721
18. Lang JW, Kong LB, Wu WJ, Luo YC, Kang L (2008) Chem Commun 35:4213–4215
19. Lu Q, Lattanzi MW, Chen YP, Kou XM, Li WF, Fan X, Unruh KM, Chen JG, Xiao JQ (2011) Angew Chem Int Ed 50:6847–6850
20. Lin C, Ritter JA, Popov BN (1998) J Electrochem Soc 145:4097–4102
21. Reddy MV, Yu T, Sow CH, Shen ZX, Lim CT, Rao GVS, Chowdari BVR (2007) Adv Funct Mater 17:2792–2799
22. Wu NL, Wang SY, Han CY, Wu DS, Shiue L-R (2003) J Power Sources 113:173–178
23. Nagarajan N, Zhitomirsky I (2006) J Appl Electrochem 36:1399–1405
24. Wu MS, Lee RH, Jow JJ, Yang WD, Hsieh CY, Weng B (2009) J Electrochem Solid State Lett 12:A1–A4
25. Wang DW, Wang QH, Wang TM (2011) Nanotechnology 22:135604
26. Xie KY, Li J, Lai YQ, Lu W, Zhang ZA, Liu YX, Zhou LM, Huang HT (2011) Electrochem Commun 13:657–660
27. Sassin MB, Mansour AN, Pettigrew KA, Rolison DR, Long JW (2010) ACS Nano 4:4505–4514
28. Singh V, Joung D, Zhai L, Das S, Khondaker S, Seal S (2011) Prog Mater Sci 56:1178–1271
29. Novoselov KS, Geim AK, Morozov SV, Jiang D, Zhang Y, Dubonos SV, Grigorieva IV, Firsov AA (2004) Science 306:666–669
30. Dikin DA, Stankovich S, Zimney EJ, Piner RD, Dommett GHB, Evmenenko G, Nguyen ST, Ruoff RS (2007) Nature 448:457–460
31. Geim AK, Novoselov KS (2007) Nat Mater 6:183–191
32. Zhu XJ, Zhu W, Murali YS, Stollers MD, Ruoff RS (2011) ACS Nano 5:3333–3338
33. Wang HL, Casalongue HS, Liang YY, Dai HJ (2010) J Am Chem Soc 132:7472–7477
34. Hummers WS, Offeman RE (1958) J Am Chem Soc 8:1339–1339
35. Wang DW, Wang QH, Wang TM (2011) Inorg Chem 50:6482–6492
36. Li D, Müller MB, Gilje S, Kaner RB, Wallace GG (2008) Nat Nanotechnol 3:101–105
37. Wu ZS, Ren WC, Wen L, Gao LB, Zhao JP, Chen ZP, Zhou MG, Li F, Cheng HM (2010) ACS Nano 4:3187–3194
38. Bai H, Li C, Shi QG (2011) Adv Mater 23:1089–1115
39. Zhang LL, Zhao XS (2009) Chem Soc Rev 38:2520–2531
40. Wang HL, Robinson JT, Diankov G, Dai HJ (2010) J Am Chem Soc 132:3270–3271
41. Yariv S, Mendelovici E (1979) Appl Spectrosc 33:410–411
42. Apte SK, Naik SD, Sonawane RS, Kale BB (2007) J Am Ceram Soc 90:412–414
43. Wu CZ, Yin P, Zhu X, Ouyang C, Xie Y (2006) J Phys Chem B 110:17806–17812
44. Zhu W, Murali S, Stoller MD, Ganesh KJ, Cai WW, Ferreira PJ, Pirkle A, Wallace RM, Cychosz KA, Thommes M, Su D, Stach EA, Ruoff RS (2011) Science 332:1537–1541
45. Fan ZJ, Yan J, Zhi LJ, Zhang Q, Wei T, Feng J, Zhang ML, Qian WZ, Wei F (2010) Adv Mater 22:3723–3728
46. Wang B, Park J, Wang CY, Ahn H, Wang GX (2010) Electrochim Acta 55:6812–6817